Materials Characterization xxx (xxxx) 112322

Contents lists available at ScienceDirect

Materials Characterization

journal homepage: www.elsevier.com/locate/matchar

Mechanical behavior of polycrystals: Coupled in situ DIC-EBSD analysis of pure copper under tensile test

J.P. Goulmy *, D. Depriester, F. Guittonneau, L. Barrallier, S. Jégou

Arts et Métiers Institute of Technology, MSMP, HESAM Université, F-13617 Aix-en-Provence, France

ARTICLE INFO

Keywords:
DIC
In situ tensile test
EBSD
Mechanical behavior
Crystal plasticity

ABSTRACT

Understanding the mechanisms at the microstructure scale is of great importance for modeling the behavior of materials at different scales. To this end, digital image correlation (DIC) is an effective measurement method for evaluating the strains generated by various loading conditions. The objective of this paper is to describe the experimental setup and the use of high resolution digital image correlation (HRDIC) during in situ Scanning Electron Microscope (SEM) tests in order to provide a coupling between polycrystalline modeling and experiment in the near future. The HRDIC technique is used to evaluate the tensile behavior of a pure copper polycrystal at room temperature. Several magnitudes are investigated in order to discuss the representativeness of the results with respect to the macroscopic scale. The selected image correlation parameters are discussed regarding the ability of the technique to define inter- and intra- granular strain heterogeneities. Finally, based on EBSD analyzes, the impact of grain orientation on the mechanical behavior is discussed. The Schmid factor, calculated from a macroscopic stress, appears to be the determining factor concerning the orientation of the location bands. On the other hand, it is not sufficient to define the mean strains in the grains.

1. Introduction

Understanding the mechanisms at the microstructure scale is of great importance for modeling the behavior of materials at different scales. This is the first step towards optimizing microstructures to improve the mechanical properties of a part. It has been demonstrated, for example, that there is a strong relationship between strain heterogeneities generated in grains and fatigue initiation on various crystalline materials [1,2]. The characterization of these heterogeneities, which can be inter- or intra- granular, is therefore of paramount importance [3–5]. For this purpose, high-resolution digital image correlation (HRDIC) is an effective measurement method for evaluating strains generated by various loading conditions [6–15]. It allows access to information at several scales: several grains, one grain or even sub-grains. This information appears essential in understanding the distribution of strains and stresses within the microstructure [2]. Several experimental studies have been previously performed on copper oligocrystals in order to define the strain mechanisms [13,16]. The advantage of using this type of material is the presence of grains whose size is larger than one millimeter. It is thus possible to identify the strain mechanisms using conventional tools, such as optical cameras with a resolution of about $5\mu m$ per pixel (μmpx^{-1}). However, differences in behavior could be observed between oligocrystals and polycrystals, whose grain size is of the order of a few tens of micrometers. It is then necessary to study also in detail the behavior of polycrystalline materials in order to model them. In this case, the use of in situ scanning electron microscope (SEM) characterization techniques is a way to increase the resolution of the measurements. Using such characterization techniques requires the implementation of a precise methodology to observe the mechanisms at sub-micrometer scales. The choice of speckle, the measurement conditions and the correlation of the images are all parameters to be considered for the successful completion of the tests [17–19]. One of the necessary considerations is the representativeness of the observations regarding the macroscopic behavior. A choice must be made between having a sufficient resolution to capture the inter- and intra- granular strain mechanisms and having a region of interest (ROI) large enough to represent the macroscopic behavior. This is even more important when the final aim of the test is to develop experiments, allowing the implementation of inverse identifications of polycrystalline models [20].

In order to understand the strain mechanisms, the electron backscattered diffraction (EBSD) technique is often coupled to the DIC [6,21]. It

* Corresponding author.
E-mail addresses: jean-patrick.goulmy@ensam.eu (J.P. Goulmy), dorian.depriester@ensam.eu (D. Depriester), fabrice.guittonneau@ensam.eu (F. Guittonneau), laurent.barrallier@ensam.eu (L. Barrallier), Sebastien.Jegou@ensam.eu (S. Jégou).

https://doi.org/10.1016/j.matchar.2022.112322
Received 22 July 2022; Received in revised form 16 September 2022; Accepted 18 September 2022
1044-5803/© 20XX

allows to get information on the orientation of the grains, or the distortion of the network within the grains. It is thus particularly useful to make the link between the Schmid factor and the slip systems activated in the polycrystal. When a slip system is activated because of shear stress, slip bands appear in the grains, corresponding to the intersection between the observation plane and the slip plane. Using DIC allows then to highlight them particularly. Therefore, many studies investigated the relationship between the Schmid factors and the strains generated in the grains by coupling these two techniques [22–26]. These studies show that, with polycrystals loaded in fatigue, a majority of crystallites with slip bands have angles in agreement with Schmid's law [22]. On the other hand, it is also mentioned that the maximum Schmid factors are not necessarily associated with the highest strains inside the grains [25–27]. Other parameters that must be considered: grain-to-grain misorientation angles, the number of active slip systems, grain size and morphology, and geometric constraints from the surrounding grains [4,5,13].

Using polycrystalline models to translate the behavior of materials is becoming more and more common. This is evidenced by the growing number of publications on the subject over the last five years [28–31]. By coupling the technique of digital image correlation to modeling, the authors have multiple objectives: to refine the understanding of the physical mechanisms at the grain scale, to develop new modeling approaches or to improve the prediction of physical models. Several approaches have been investigated in the literature, notably the emergence of crystal plasticity finite element (CPFE) models [28,32–34] and crystal plasticity peridynamic (CPPD) models [29,35,36]. On the basis of the polycrystalline models, two approaches are opposed, Sachs' and Taylor's [37,38].

The experiments performed before the modeling must provide representative data of the macroscopic behavior in order to identify the parameters of a polycrystalline model in a minimum of time. The choice of experimental parameters and the analysis of the results represent a significant way to reduce the optimization costs. How to define the approach scale for analysis? Which resolution should be adopted? Is the ROI large enough to represent the macroscopic behavior? Which information is needed to make a choice of modeling? Answering these questions is of great interest when one wishes to set up a coupling between experimentation and modeling. If many studies coupling DIC and finite element modeling are present in the literature, the choice of the parameters is few discussed and is often done by experience.

The objective of this paper is to describe the experimental setup and the use of HRDIC during in situ Scanning Electron Microscope tests in order to provide a coupling between polycrystalline modeling and experiment. The influence of DIC parameters on the ability of such analysis to track local phenomena (e.g. localization) in a strained polycrystal is investigated. For the special case of pure copper, an optimal set of parameters is proposed, allowing to study the shear bands occurring during an in situ tensile test.

The material and the characterization methods are presented in Section 2. Section 3.1 aims to define the DIC parameters, allowing the observation of inter- and intra- granular heterogeneities through a sensitivity study. During the tensile test, images were captured at two different magnifications to get different resolutions and fields of view. Section 3.2 is dedicated to the comparison of results obtained with these two resolutions based on the number of grains, texture and average strain values. The results from DIC are analyzed in Section 3.3. The combination of EBSD and DIC data is then especially useful for understanding the link between strain and crystallographic orientation of grains. Finally, a discussion is proposed in Section 4. The minimum number of grains to be considered for performing the analysis, the choices of DIC parameters and the variables of interest are discussed in this section.

2. Materials and methods

2.1. Material

The material used in this study was commercially pure copper (99.9%). Its chemical composition, measured by optical emission spectroscopy using a SPECTROMAXx LMM05 (ICP-OES) is given in Table 1. The as-received material was rolled sheet. Thus, an homogenization heat treatment of 500°C for 30 min followed by water quenching was performed. The heat treatment parameters were chosen to achieve an homogeneous microstructure with an average grain size of approximately $10\mu m \pm 6\mu m$ (see histogram in Fig. 11). This grain size was defined as a compromise between: 1) a grain size large enough to observe inter- and intra- granular localization phenomena; 2) a grain size small enough to have a sufficient number of grains in the digital image correlation analysis field to be representative of the macroscopic behavior of the material. This last issue will be discussed in Section 4. Note that some twins are present in the microstructure (see Fig. 1). They are of thermal origin. They were created during the homogenization heat treatment. This particularity has not been investigated in the following article.

2.2. Microstructural characterization

Prior to microstructure observations, the specimen was mechanically ground and polished down to a diamond polishing paste of $1\mu m$. A chemical etch composed of $2.5\ mL FeCl_3$ (41%), $10\ mL$ HCl (37%) and $100\ mL\ H_2O$ was used for 30 s to reveal the intra-granular microstructure. The choice was made not to deposit speckles on the surface of the specimens in order not to degrade the EBSD acquisition [39]. Chemical etching allowed the generation of small markers whose size was between 100 and $200\ nm$ (see Fig. 1.c). A pre-test analysis showed that the markers induced by chemical etching were adequate for applying DIC at high resolution [40].

The images were acquired using a FEG JEOL JSM-7001F in high vacuum (HV) mode. The working distance ($12.1\ mm$), was imposed by using an in situ tensile test device (see Section 2.3). The image size ($1280 \times 1056\ px$) was also required by the choice of integrating the images. An integration of images (8 in the present work) allows to increase the signal to noise ratio. Finally, dwell time ($2.89\ \mu s$), acceleration voltage ($10\ kV$) and probe current number (9 a.u.) were set because an increased stability of the images was obtained with these parameters.

Two magnifications were investigated during the mechanical tests: $300\times$ and $5000\times$. The acquisition of images at $300\times$ magnification allowed a "macroscopic" view of the microstructure with a measurement field of $4096 \times 3072\ \mu m$ and a resolution of $3.2\ \mu m px^{-1}$. In the following, images acquired at $300\times$ magnification are referred to as Low Resolution images (LR). Thus, it was possible to determine the macroscopic strain applied to the specimen during the test (see Section 3.2). The acquisition of the images at a magnification of $5000\times$ gave a resolution of $19\ nm px^{-1}$, allowing to highlight inter- and intra- granular strain sites during the mechanical loading (see Section 3.1). In the following, images acquired at $5000\times$ magnification are referred to as High Resolution images (HR). To obtain a number of grains greater than 100 in the field of observation, a stitching of several images at this resolution was required. The impact of the number of grains on the results is discussed in detail Section 4. At the end, 8×6 images were captured (a total of 48 images per loading step) at high resolution. A 10% overlap between im-

Table 1
Chemical composition of the material (weight percentage).

	Cu	P	Sn	Pb
MEAN	99.892	0.038	0.011	0.011
STD	0.010	0.001	0.001	0.001

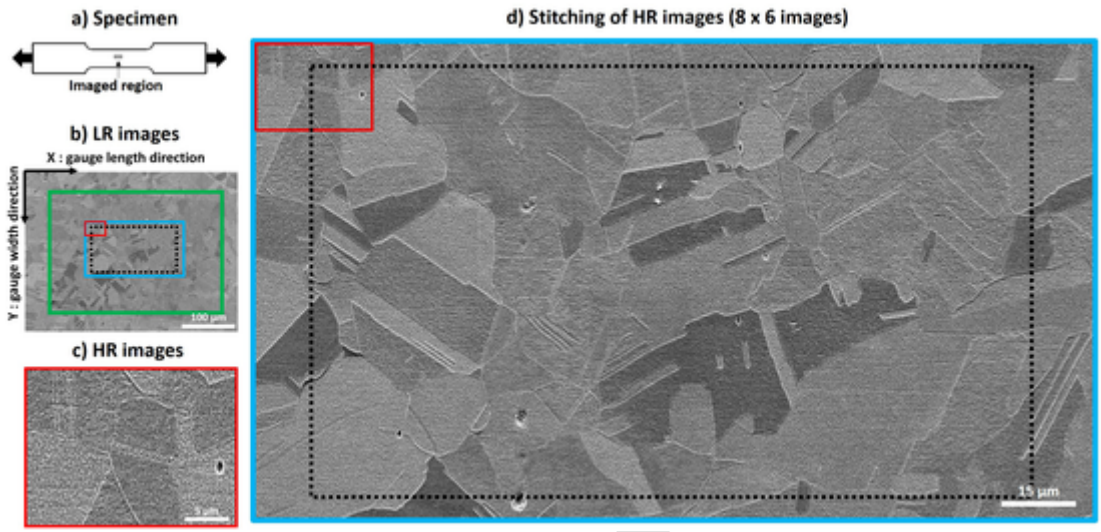

Fig. 1. a) Specimen. Examples of captured images: b) at low resolution (LR), c) at high resolution (HR) and d) after stitching of high resolution images. Blue rectangle: image obtained after stitching. Red rectangle: HR image. Green rectangle: EBSD acquisition area (noted Full area). Black dotted rectangle: area selected for image correlation analysis and EBSD (noted DIC area).

ages was used. The images were stitched using the macro grid collection stitching module with linear Blending in ImageJ software [41]. The final image resulted in a measurement field of 177×100 µm (9316×5263 px). Examples of images obtained at these two resolutions, as well as the stitching performed from the HR images are shown in Fig. 1.

For EBSD acquisition, SEM conditions were: acceleration voltage 15 kV, objective lens aperture 50 µm, probe current number 16 (a.u.), magnification 300× and tilt angle 65°. EBSD maps were acquired using a HKL Nordlys camera driven by Channel 5 software (with Flamenco module) from Oxford Instruments. The camera resolution was binned by 4 using a low gain and an averaging of 4 images in order to minimize noise. Resolution in Hough space was 100 pixels; between 6 and 9 bands were detected in each Kikuchi pattern and the step size was 300 nm for a grid 1362×1021 px.

The EBSD dataset was processed using the MTEX v5.2 toolbox for MATLAB® [42]. The Grain Orientation Spread (GOS) is usually considered as a qualitative descriptor of work hardening of grains [43,44]. For a given grain k, it is defined as:

$$\mathrm{GOS}(k) = \frac{1}{J(k)} \sum_{i \in \mathrm{grain}k} \mathrm{ang}\left(\bar{g}_k, g_i\right) \tag{1}$$

Where $\mathrm{ang}\left(\bar{g}_k, g_i\right)$ denotes the misorientation angle between pixel i (g_i) and the mean orientation of grain k ($\bar{g}_k$), whereas $J(k)$ is the number of pixels in grain k. Likewise, the Grain Average Misorientation (GAM) is defined as the arithmetic mean of the Kernel Average Misorientation (KAM):

$$\mathrm{GAM}(k) = \frac{1}{J(i)} \sum_{i \in \mathrm{grain}k} \mathrm{KAM}(i) \tag{2}$$

With

$$\mathrm{KAM}(i) = \frac{1}{p} \sum_{j \in \mathrm{N}_p(i)} \mathrm{ang}\left(g_i, g_j\right) \tag{3}$$

Where $\mathrm{N}_p(i)$ denotes the p-connected neighborhood of pixel i. A p value of 5 was used in this work.

EBSD data can be used to compute the Orientation Distribution Function (ODF) [42]. One can define the change in ODF between the starting texture (ODF_0) and the deformed material ($\mathrm{ODF}_{\mathrm{def}}$):

$$\Delta\mathrm{ODF} = \mathrm{ODF}_{\mathrm{def}} - \mathrm{ODF}_0 \tag{4}$$

In the following, two analysis areas are used: one area corresponding to all the data acquired in EBSD (named full area hereafter) and another one corresponding to the area analyzed in DIC (smaller than the EBSD and named DIC area hereafter) (see Fig. 1). 454 grains were reconstructed in the full area whereas 115 grains were reconstructed in the area retained to perform DIC.

The mesh obtained from ESBD differing from the pixel grid of the image captured by SEM, an interpolation of the EBSD values at each pixel of the image taken at step 0 was performed to reconstruct the grain boundaries on the DIC maps.

2.3. Mechanical characterization

The in situ SEM tensile test was performed using a Kammrath and Weiss 5 kN machine. The specimens had a cross-section of 1.75×6 mm and a gauge length of 16.4 mm. The stress axis was oriented along the X-axis (horizontal) for all strain maps and images (see Fig. 1). The loading was applied with a displacement rate of 70 µm/ min and was paused at 3 steps to perform intermediate microscopy work. Fig. 2 illustrates the time-evolution of engineering stress, measured from the tensile ma-

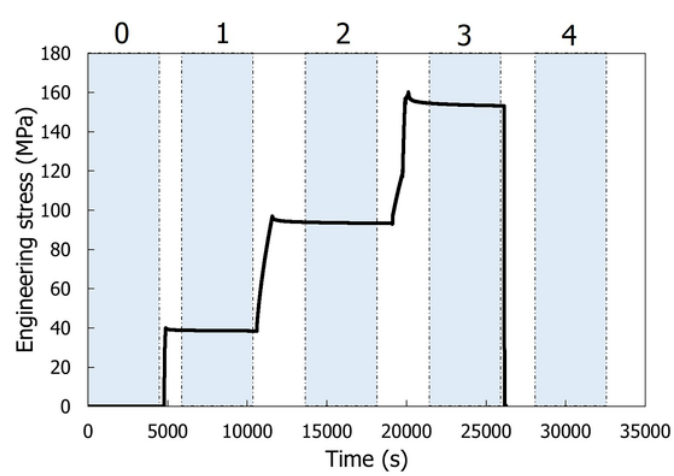

Fig. 2. Evolution of engineering stress versus time during the tensile test. The blue areas represent the time needed to capture images for each step.

chine. At each step, the displacements were held constant and the evolution of the stress was recorded. The acquisition time of a set of images was approximately 75 min. It was observed that an increase in the applied strain induced an increase in the stress relaxation during the measurement steps. As expected, the largest stress variation was observed at the beginning of the steps. In order not to be impacted by relaxation effects, which can influence the measurements [21], a waiting time was applied before each image was taken, thus allowing a stable mechanical field over time. Table 2 sums up the stress level measured at the beginning and end of each step. The maximum stress variation observed during imaging was less than 1.3 MPa. In addition, in order to evaluate whether the DIC measurements varied during the duration of the step, images at 300× magnification were taken at the beginning and at the end of each step.

2.4. Digital Image Correlation measurements

The images were correlated using the Ncorr software [45]. The subsets used were circular. An analysis window size φ_{window} was calculated in order to study the influence of image correlation parameters. Each image was a regular grid of pixels, as schematically illustrated in Fig. 3. The calculation of strain fields by DIC was performed in two steps. The first step was to calculate the displacement fields. Depending on the selected parameter P_{spacing}, the number of pixels of the image for which the calculation is performed is different ($P_{\text{spacing}} = 2$ px in Fig. 3). Thus, in the case shown in Fig. 3, only the black pixels are calculated. P_{spacing} equals zero means that a calculation is done for each pixel of the image. The displacements of each black pixel are determined from the calculation of all the pixels located in the associated blue subset. Its size is set by a parameter R_{subset} ($R_{\text{subset}} = 4$ px in Fig. 3). A new network of pixels, named here pseudo-pixels, is thus created to represent the displacement maps. The size of each pseudo-pixel is dependent on the subset spacing selected previously. The second step of the analysis consists in calculating the strains from the displacement field previously obtained. The calculation of the strains is done from the displacement fields of all the pseudo-pixels in the purple subset. The size of this subset is defined by a parameter R_{strain} (equal to 3 pixels in Fig. 3). The analysis window corresponding to the pixels having an influence on the displayed strains for a pixel of the image, is defined in Eq. (5) and represented in red in Fig. 3.

$$\varphi_{\text{window}} = \left[\left(2R_{\text{subset}} + 1\right) + \left(2R_{\text{strain}}\left(P_{\text{spacing}} + 1\right)\right)\right] \times \text{resolution} \tag{5}$$

Given the displacement field $\mathbf{u}$, the 2nd order gradient tensor F is computed as follows:

$$F_{ij} = \frac{\partial u_i}{\partial X_j} + \delta_{ij} \tag{6}$$

where X_j denotes the initial coordinate along the j-th axis in the reference image, and δ is the Kronecker delta. Neglecting out-of-plane strains, Di Gioacchino et al. have introduced the effective shear strain [6]:

Table 2
Values of the stresses and strains recorded during the image acquisition.

Step	1	2	3	4
Start–end values of engineering stress (MPa)	39.2–38.5	96.4–93.3	159.1–152.1	0
Start–end values of engineering stress during image capture (MPa)	38.9–38.5	93.9–93.3	154.5–153.2	0
Start–end values of true strain for LR images (%)	0.39–0.41	4.35–4.36	14.34–14.38	14.09
Value of true strain for HR images (%)	0.37	4.47	14.56	14.24

$$\gamma_{\text{eff}} = \sqrt{\left(F_{11} - F_{22}\right)^2 + \left(F_{12} + F_{21}\right)^2} \tag{7}$$

Note that these authors actually used a 1/2 factor in the original paper for the definition of γ_{eff}. For the sake of consistency with the notation ("γ" usually relates to the engineering shear strain), the definition given in (7) is used for γ_{eff} throughout this paper. Nevertheless, since γ_{eff} is usually used for comparative purposes in order to highlight strain heterogeneities, this factor does not influence the analyzes. However, (7) is only valid under the small strain assumption[1], thus it should be used with caution in large strains. As a result, an alternative descriptor was used in this work, called equivalent shear and defined as follows:

$$\gamma_{\text{eq}} = \sqrt{\frac{3}{2}}\sqrt{\sqrt{1 + 4\varepsilon_{\text{eq}}^2} - 1} \tag{8}$$

where ε_{eq} denotes the von Mises equivalent strain, with:

$$\varepsilon_{\text{eq}} = \sqrt{\frac{2}{3}}\sqrt{\frac{(E_{11} - E_{22})^2 + (E_{11} - E_{33})^2 + (E_{22} - E_{33})^2}{3} + 2E_{12}^2} \tag{9}$$

In (9), E_{ij} denotes the components of the Green–Lagrange (GL) tensor, so that:

$$E_{11} = \frac{F_{11}^2 + F_{21}^2 - 1}{2} \tag{10a}$$

$$E_{12} = \frac{F_{11}F_{12} + F_{21}F_{22}}{2} \tag{10b}$$

$$E_{22} = \frac{F_{12}^2 + F_{22}^2 - 1}{2} \tag{10c}$$

$$E_{33} = \frac{\left(F_{11}F_{22} - F_{12}F_{21}\right)^{-2} - 1}{2} \tag{10d}$$

Details behind Eqs. (8), (9) and (10d) are provided in Appendix A.

In the following, the average equivalent shear strain calculated over the entire field is noted $\langle\gamma_{\text{eq}}\rangle$. The average equivalent shear strain calculated for each grain is noted $\overline{\gamma_{\text{eq}}}$. The average of $\overline{\gamma_{\text{eq}}}$, calculated on all grains, is noted $\langle\overline{\gamma_{\text{eq}}}\rangle$.

3. Results

3.1. Definition of digital image correlation parameters for high resolution images

In order to identify which DIC parameters should be used in the following, a sensitivity study was conducted to address two requirements. The DIC analysis must allow to define the localization of inter- or intragranular heterogeneities and to get quantitative values of the strains in each grain. The three parameters studied were: $R_{\text{subset}}, R_{\text{strain}}$, and P_{spacing} previously defined in Fig. 3. In order to identify the influence of these parameters on the ability of the technique to define the strain heterogeneities, different profiles were drawn in the images to extract the γ_{eq} values along the axis. The results appeared independent of the grain analyzed. It was therefore chosen to represent only the results of a single grain (# 103).

In order to identify the impact of these parameters on the quantitative values, $\overline{\gamma_{\text{eq}}}$ and $\langle\overline{\gamma_{\text{eq}}}\rangle$ values were also calculated and compared.

As a first approach, the parameters $R_{\text{subset}}, R_{\text{strain}}$, and P_{spacing} were modified such that φ_{window} was set to an arbitrary value of 1.3 μm. Fig. 4 shows the equivalent shear strain maps γ_{eq} for step 2. No significant difference is observed for the various selected correlation parameters. These results are confirmed more quantitatively with the profile plots

[1] Eq. (7) is actually based on the calculation of principal strains from the infinitesimal strain tensor.

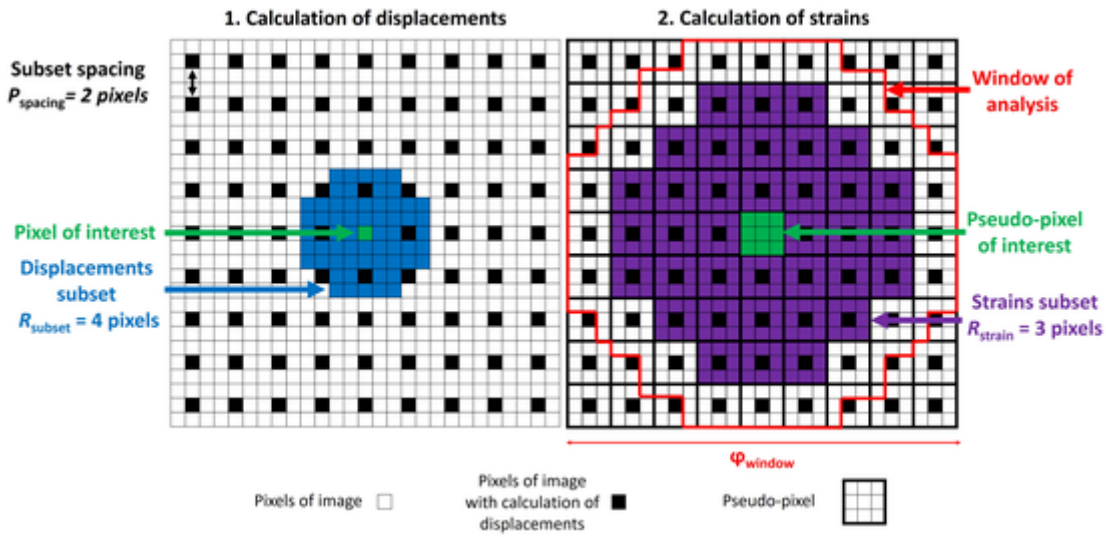

Fig. 3. Schematic representation of the DIC parameters: displacement subset, strain subset and window of analysis.

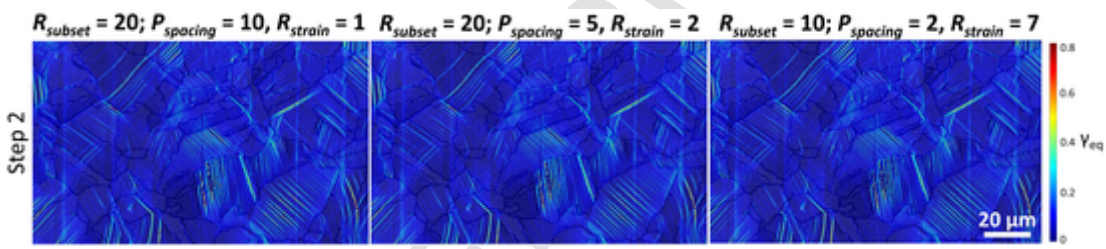

Fig. 4. Maps of γ_{eq} obtained for different DIC parameters, φ_{window} equal to 1.3 µm. Applied loading: step 2.

for the first three loading increments (Fig. 5). The differences are relatively small for steps 1 and 2. At larger strains (step 3), differences appear, although it is still impossible to precisely define the impact of the different parameters. Because of these small differences, it was chosen to discuss only the influence of a single, global parameter φ_{window} to identify the image correlation parameters to be used in the following. Furthermore, the amount of indexed pixels during the DIC analysis somewhat depend on the selected correlation parameters. An indexed pixel is a pixel from the reference image that was found in an image acquired during loading. The larger the size of the R_{subset}, the larger the percentage of indexed pixels. For a given window size φ_{window}, it is therefore better to use the largest R_{subset} value as possible. Also, the number of indexed pixels depends on the applied load, with a decrease when the value of the macroscopic strains is increased. This result was expected due to the high strain applied between the two steps. The rate of indexed pixels for the largest loading is still higher than 99%, which validates the protocol of image acquisition and analysis implemented.

In order to identify the influence of φ_{window} on the results, five window sizes were arbitrarily selected: 0.54 µm, 1.3 µm, 3 µm, 5.2 µm, 9.6 µm. Fig. 6 shows different maps of γ_{eq} as a function of φ_{window} for the step 3. When the window size is larger than 1.3 µm, the localization of slip bands inside the grains is barely visible. The largest strains, located at the grain boundaries, remain diffusely visible. Beyond a window size of 5.2 µm, the strain heterogeneities almost vanish in the whole microstructure. Compared to the DIC maps, the HR image is shown in Fig. 6. Some slip bands are clearly visible directly on SEM micrographies. Their width is between 100 and 200 nm. On the other hand, other slip bands are not observed on the SEM images but are detected by DIC.

Fig. 7 shows the γ_{eq} profiles obtained for different window sizes φ_{window} and different loading steps. Peaks, characteristic of slip bands inside the grain, appear as early as step 1. Their number and intensity increase as the load increases. When the applied loading is low (step 1), the noise generated when using the window size φ_{window} of 0.54 µm appears important regarding the maximum value. The ratio between the standard deviation and the mean value of the equivalent shear strain is around 0.25. On the other hand, the noise becomes negligible at further steps (steps 2 and 3). For these loads, a significant increase in the mean value of the strains is observed while the measurement noise remains constant or does not increase as much (the ratio between the standard

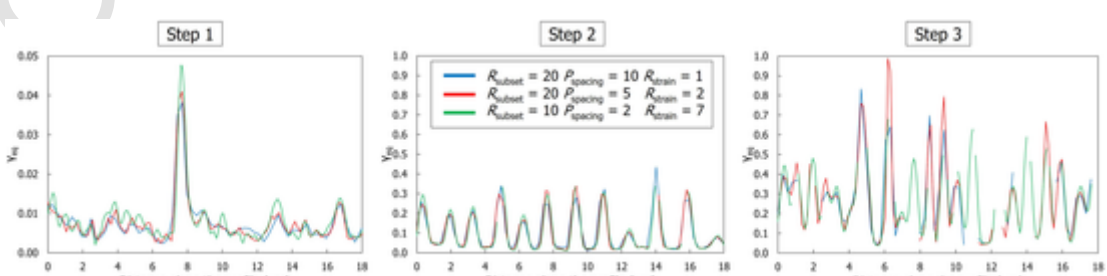

Fig. 5. Profiles of γ_{eq} depending on the loading step and the DIC parameters (with φ_{window} = 1.3 µm).

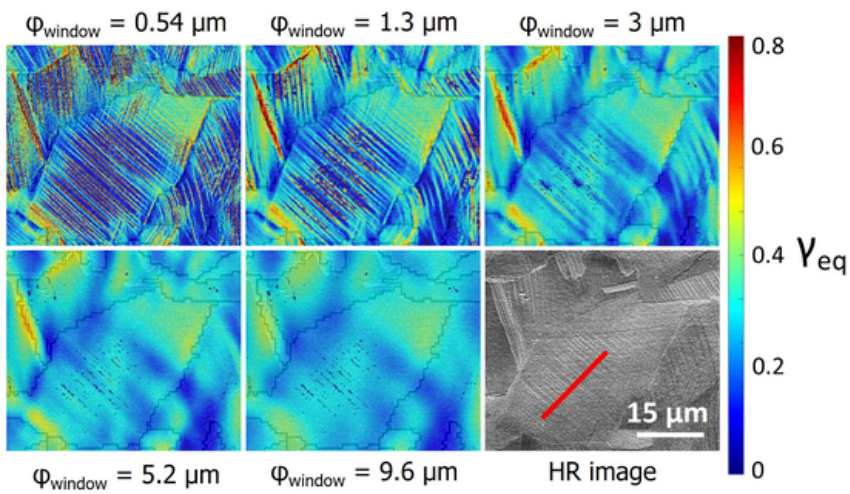

Fig. 6. Influence of the analysis window size φ_{window} on γ_{eq} maps, step 3. The red line on SEM image represents the profile used to plot the γ_{eq} values along an axis.

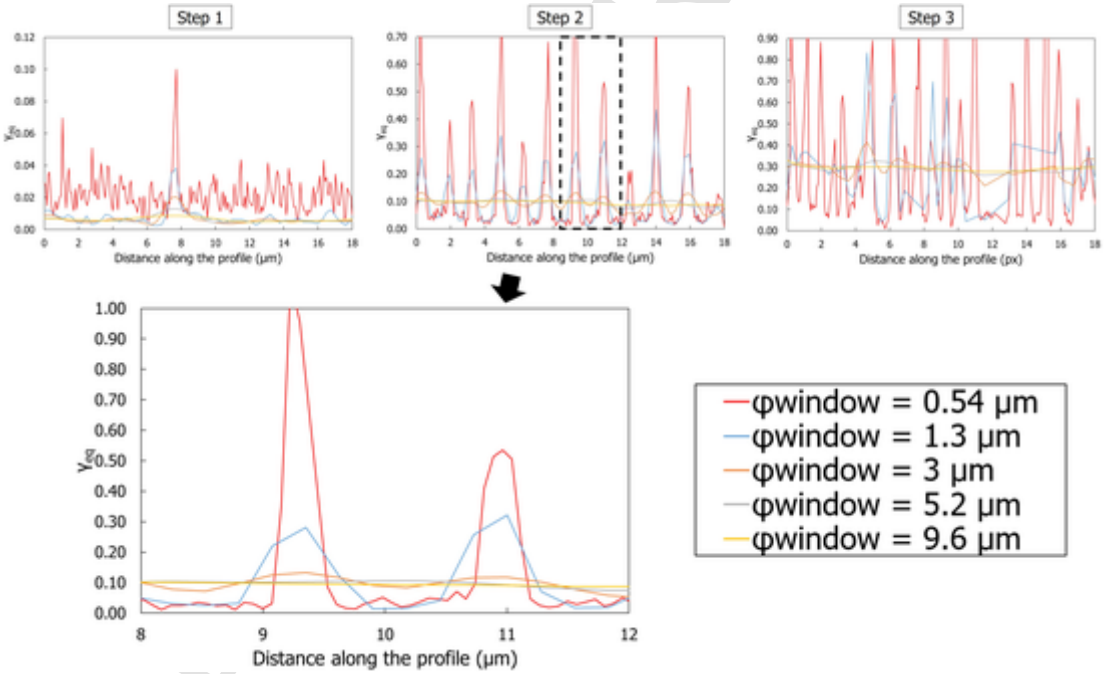

Fig. 7. Profiles of γ_{eq} obtained for different window sizes φ_{window}.

deviation and the mean value of the equivalent shear strain is around 0.05).

The width of the observed peaks in Fig. 7 decreases as φ_{window} decreases. Moreover, when φ_{window} is greater than 3 μm, two very close slip bands are no longer detectable during step 3. The choice of the analysis window has therefore an essential role in the definition of the slip bands (their presence and width). For the smallest analysis window, the width of the peaks is around 300 nm. This value is higher than the band widths observed directly on the SEM images.

The position of the peaks is not affected by the selected analysis window. The definition of the spacing between the slip bands is therefore independent of the window size as long as the slip bands are detectable.

The amplitude of the peaks generated by the slip bands also depends on the size of the analysis window. Outliers are obtained for the smallest analysis window without the ability to validate the values obtained by the other windows. Since the correlation of the images is performed with high accuracy and independently of the analysis window, it is possible to consider that the speckle is well adapted to the measurements carried out here and has limited impact on the results. Extensive experimental observations such as transmission electron microscopy characterizations could define the width of the slip bands precisely. However, to our knowledge, no common means of measurement can effectively define the amplitude of strains in the slip bands. The application of DIC is challenged by the small size of the slip bands relative to the resolution used and their uniform appearance. Using larger magnitudes and a speckle smaller than the localization bands would be necessary between each loading step to effectively evaluate the strains generated at these locations in the material. The values obtained in the present work can therefore be used for comparison purposes only.

The value γ_{eq} calculated between the localization bands is also clearly affected by the analysis window size φ_{window}. The larger the window size, the higher the value between the slip bands. This result is related to the strain generated by the slip bands, which are averaged out as soon as the analysis window is large.

A comparison of the $\overline{\gamma_{eq}}$ values calculated in each grain for three loading increments and the five analysis windows is given in Fig. 8. At the early deformation stage (step 1), $\overline{\gamma_{eq}}$ varies with the window size. A

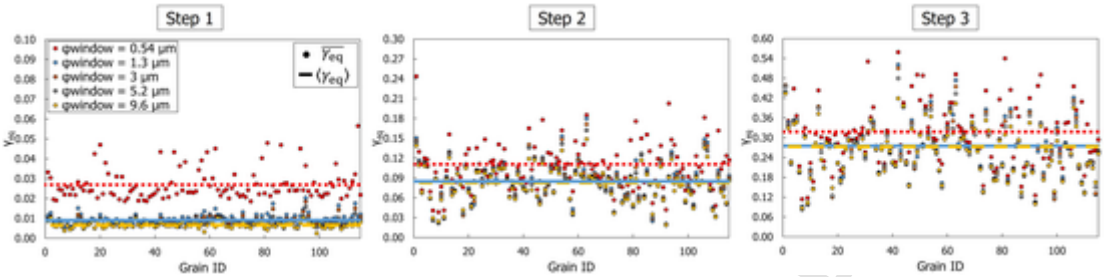

Fig. 8. Circles: average values measured in each grain $\overline{\gamma_{eq}}$, lines: average values measured in each image $\langle \gamma_{eq} \rangle$, for the three loading steps (1, 2 and 3) and function of the analysis window size φ_{window}.

notable gap is obtained between the smallest window φ_{window} equal to 0.54 µm and the others. At further steps, this gap becomes small compared to the average value. The average value $\overline{\gamma_{eq}}$ calculated in each grain becomes less dependent on the window size. This result can be related to the observations made in Fig. 7. The high noise obtained with window size φ_{window} equal to 0.54 µm as well as the high values, calculated at the location bands, generate an artificial increase of the mean value in the grains. As an example, the $\overline{\gamma_{eq}}$ maps computed in each grain for step 3 are shown in Fig. 9 for each value of φ_{window}. The size of the analysis window plays a minor role in the values obtained, especially when it is larger than 1.3 µm.

Considering all these results, it appears necessary to have a multiscale approach to the problem. Using a window size of the order of five times the width of the slip bands (φ_{window} = 0.54 µm) allows to visualize them, and to evaluate their width and spacing. In contrast, the average values obtained per grain or for an entire measurement field are too noisy and affected by aberrant values within the slip bands to be used. A larger correlation window has to be used to calculate average values within the grains and for the whole measurement field. It was shown that a window size larger than about ten times the width of the slip bands (φ_{window} = 1.3 µm) suffices to have minimum effect on the values measured in the slip bands. Thus, the definition of the slip bands could be achieved through the use of a window size φ_{window} equal to 0.54 µm while the average values would be calculated using a window size φ_{window} equal to 1.3 µm. A larger window size could have been selected, but the value mentioned earlier allows the visualization of the slip bands without deteriorating the average values. Finally, for a given window size, the largest possible value for R_{subset} should be selected to limit the number of non-indexed pixels. In the following, all the results were obtained with a window size φ_{window} equal to 1.3 µm for HR images. The following DIC parameters were used: R_{subset} = 20 px, R_{strain} = 1 px, and $P_{spacing}$ = 10 px.

3.2. Comparison between macroscopic, LR and HR images results

The objective of this section is to compare results obtained with LR and HR images to define a region of interest representative of the macroscopic behavior.

3.2.1. Tensile curve and DIC analyzes

The correlation of LR images appeared slightly more delicate than for HR images. The choice of the subset had to be done in relation to the ability of the technique to identify patterns in the image. However, for two images taken at the beginning or at the end of each step, the correlation of the images could be very different depending on the image correlation parameters. These results indicate that the absence of additional speckle on the surface of the samples is detrimental to image correlation for LR images. A multiscale approach is then difficult to implement. However, an influence study similar to the one presented above was done to determine the optimal DIC parameters for LR images. Hence, the parameters retained for the analysis were the following: R_{subset} = 40 pixels, $P_{spacing}$ = 5 pixels, and R_{strain} = 5 pixels. Thus, the size of the analysis window φ_{window} was about 300 µm.

Fig. 10 shows the macroscopic stress–strain curve obtained by comparing the average strains calculated from the LR images and HR images. A typical behavior of copper is obtained with a Young's modulus of about 110 GPa and a 0.2% yield strength equal to 40 MPa. The results obtained for the LR images and HR images were analyzed in detail and, as summarized in Table 2. A change in elongation of less than 0.04% is achieved between the beginning and the end of the loading step. This value also corresponds to the gap measured between two images taken successively during step 4 (zero stress). It is therefore considered that these values represent the measurement uncertainty. The results are also in agreement with the macroscopic tensile curve obtained by considering the global elongation of the specimen and the results obtained for HR images with an analysis window φ_{window} equal to 1.3 µm. The methodology set up for the image acquisition is thus validated. The calculated true strain obtained for HR images is slightly larger for the larger strains. These results were expected due to the use of a smaller

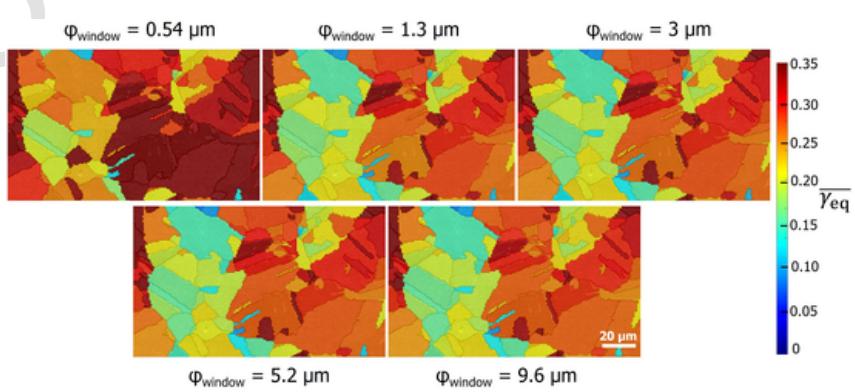

Fig. 9. Values for $\overline{\gamma_{eq}}$ maps depending on window size φ_{window} (step 3).

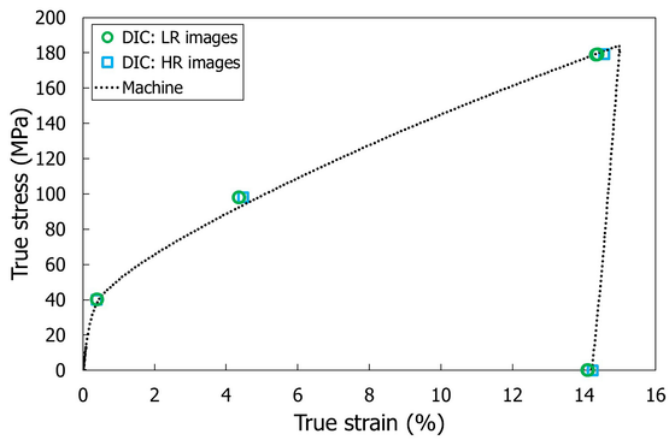

Fig. 10. Macroscopic Stress–strain curve. Comparison between machine data, and DIC performed on LR images and on HR images.

window size for HR images by a ratio of 231 (1.3 μm versus 300 μm). With a larger window, it is not possible to detect the strain sites, which necessarily generates a lower average value. However, because the results are relatively close, the interest in using LR images may appear limited.

3.2.2. EBSD consideration

In order to validate the ROI used by DIC for the HR images, the size of the grains and their crystalline orientation were investigated in two distinct areas: the area characterized by EBSD (noted full area) and the area characterized by DIC, smaller than EBSD and noted DIC area (see Fig. 1). Fig. 11.a shows a frequency histogram of the grain size for the two considered areas. Although the number of grains is reduced by a factor of three for the DIC area compared to the full area (115 grains versus 454 grains), a similar grain size distribution is obtained for both areas. The average grain diameter is approximately the same for both areas (10.1 μm for the DIC area and 11.7 μm for the full area).

Fig. 11.b illustrates Pole Figures (PFs) reconstructed from ΔODF (see Section 2.3) for the two investigated areas. A characteristic pattern of a tensile test is obtained for both areas of interest displaying (001) and (111) poles toward the loading direction and ring-like distribution for the (110) and (111) planes [46,47] in transverse plane. These results are consistent with those obtained by DIC, showing that the analysis field is representative of the macroscopic behavior of the material. This comparison allows to validate that the measurement field defined with stitched HR images is large enough to obtain an average behavior of the grains and is characteristic of the macroscopic behavior of the material. Hereafter, only the DIC area is used to comment on the results.

If the DIC area is representative of the macroscopic behavior, a question remains concerning the minimal number of grains to be considered in the analysis. The characterization of a too small area could lead to a wrong interpretation of the results and, subsequently, to an identification of the polycrystalline model parameters that are not representative of the macroscopic behavior. On the other hand, choosing a ROI that is too large would lead to an increase in measurement and computational time. This issue is further discussed in Section 4.

3.3. Analysis of region of interest

3.3.1. Strain heterogeneities and Schmid factor relationship

The strain heterogeneities generated during the tensile test within the microstructure are now being investigated. Fig. 12 shows the values of γ_{eq} as 2D maps for each loading step. These maps highlight the presence of strain localization between and within grains. At early deformation stages (step 1 and step 2), a significant localization of strains is observed. For some grains (noted A and B in the Fig. 12), significant strains are localized near or parallel to the twin boundaries. It was not possible to determine the exact origin of these strong strains. These phenomena are classically observed in polycrystalline materials with relatively high elastic anisotropy [5]. In the step 1, step 2 and step 3, the observed strains can be elastic or plastic. Because the strains are still visible in step 4, this indicates that the strains observed in grains A and B are mainly plastic. It is noticeable that the traces of the most active slip systems form an angle greater than 60° with the surrounding grains (see Fig. 13). Also, these grains are located between grains having very close orientations (see grain # 79 and grain # 93 for grain A, for example). However, other similar configurations did not result in such a significant localization of the strains (grain C between grains # 77 and # 88 for example). Therefore, we cannot rule out the possible influence of the size and shape of the grains as well as what is happening inside the material. A more extensive statistical study would be necessary to answer this difficult question.

The results obtained in DIC are then compared to the EBSD data. Fig. 13 shows a map illustrating the highest Schmid factor values in each grain, calculated by considering a constant macroscopic stress for all grains. The blue solid line represents the trace of the first active slip system, the green dashed line represents the second most active slip system, and the red dashed line represents the third most active slip system. All maximum Schmid factors are greater than 0.36. For all the results, the traces observed in DIC are oriented in the same way as the slip system, with the maximum Schmid factor SF_{max} calculated using EBSD. These results are consistent with observations made on other materials [22]. Then, when two traces are detected in the same grain, the active slip systems represent the two highest values of Schmid factor with few exceptions. For example, grain # 88 actually activated the 1st and 3rd most active slip planes (see Table 3 for references). This grain has the

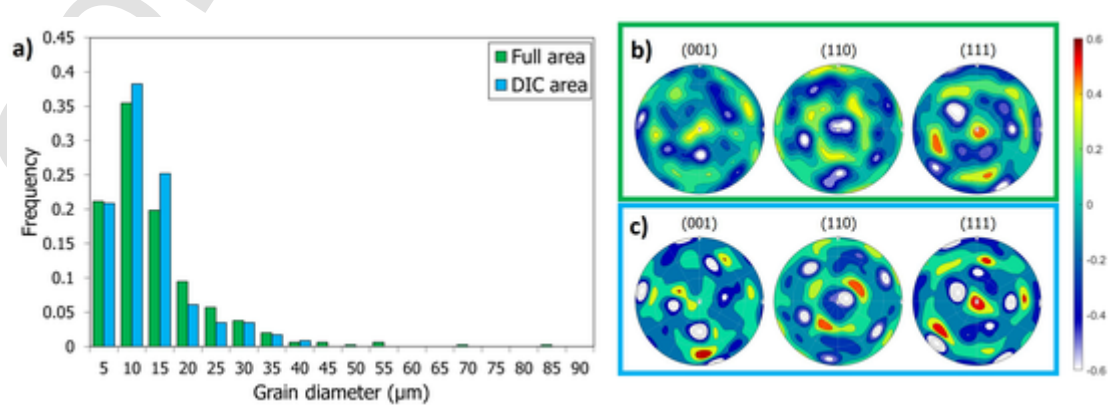

Fig. 11. a) Grain size histograms for full area and DIC area, b) PFs illustrating the changes in ODF before and after test for full area, c) PFs for the DIC area; tensile direction is out-of-plane.

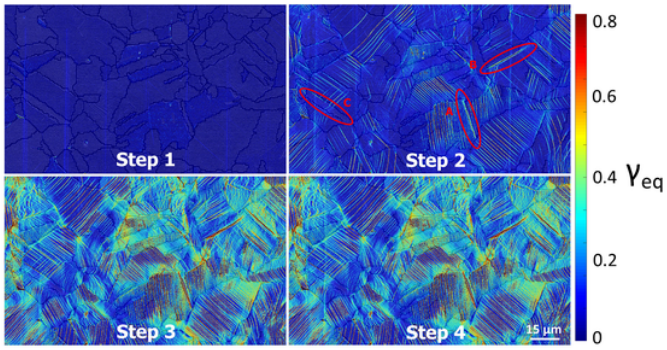

Fig. 12. Maps of γ_{eq} achieved for each loading step. Window size $\varphi_{window} = 0.54$ µm.

specificity of having four slip systems with Schmid factors between 0.42 and 0.46 which can explain these observations (Table 3). This case could also have occurred for grain # 77 where the slip systems have very close Schmid factor values (0.46 for the most important and 0.41 for the 4th). However, in this case, the two most active slip systems were indeed activated. These results show that the Schmid factor is not the only parameter to be taken into account to determine the activity of slip systems. Nevertheless, these behaviors represent a small percentage of the studied grains. Grain # 103 also has the peculiarity of activating the third sliding plane with the highest value of Schmid factor. The two first ones present similar traces; it is thus not possible to determine by DIC analyses if they were both active. The presence of a large number of traces oriented in the direction of the first two slip systems with maximum Schmid factors could suggest that both systems were indeed activated. This point will be discussed in more detail later.

The number of active systems in the grains is now discussed. Table 4 summarizes, for each step, the grains with zero, one or more than two active slip systems according to the orientation of the traces obtained in the grains in DIC. The grains for which slip bands appear for the first time are reported in bold. The grains for which the number of slip planes has increased between two stages are shown in italics. For the sake of readability, only a few grains have been reported for steps 2 and 3.

For step 1, only eight grains show slip bands and only one system appears to be active in each grain. The maximum values of SFs are plotted as a function of grain number in Fig. 14. A distinction is made between grains displaying localization bands (purple circles) and those with none (green circles). It appears that the slip activity is not correlated with the larger SFs. The notion of Schmid factor alone is therefore insufficient to predict the activity of the slip planes in the microstructure.

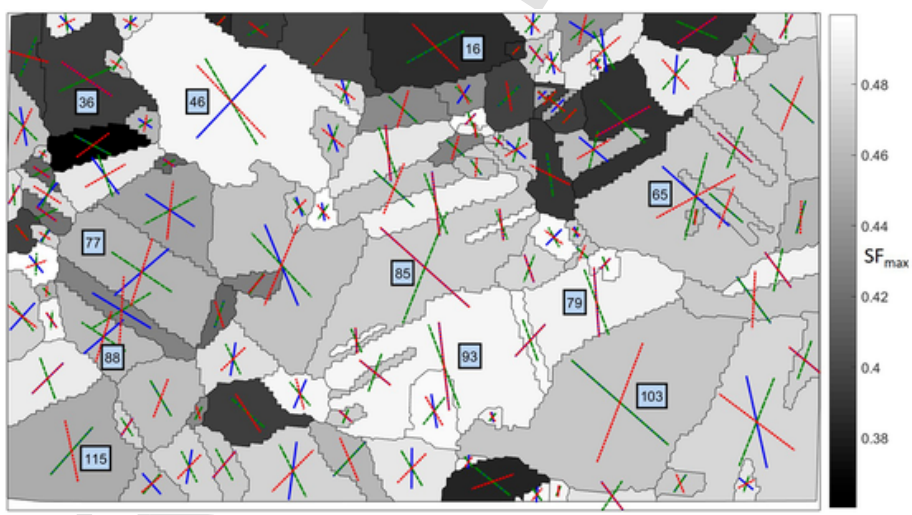

Fig. 13. Values of SF_{max} (grayscale) in each grain. The blue, green and red lines represent the first, second and third slip system in decreasing order of Schmid factor values. The grains subject to a particular analysis have their number surrounded by a black rectangle.

Table 3
Schmid factor values for selected grains. Active slip systems according to the DIC are reported with # symbol. Slip planes assumed to be active from the density of slip bands in the grains are reported with ∗ symbol. The blue, green and red values represent the first, second and third slip system in decreasing order of Schmid factor values.

	(111)			$(11\bar{1})$			$(\bar{1}11)$			$(1\bar{1}1)$		
	$[\bar{1}01]$	$[1\bar{1}0]$	$[01\bar{1}]$	$[1\bar{1}0]$	$[0\bar{1}\bar{1}]$	$[\bar{1}0\bar{1}]$	$[01\bar{1}]$	$[\bar{1}0\bar{1}]$	$[\bar{1}\bar{1}0]$	$[\bar{1}01]$	$[0\bar{1}\bar{1}]$	$[\bar{1}\bar{1}0]$
Grain ID	SS1	SS2	SS3	SS4	SS5	SS6	SS7	SS8	SS9	SS10	SS11	SS12
16	0.320	0.072	0.248	0.195	0.068	0.127	0.326	0.062	**0.388#**	0.131	0.010	0.121
36	0.004	0.082	0.078	0.357	0.094	0.263	**0.397#**	0.307	0.090	0.040	0.225	0.185
46	0.362	0.212	0.150	0.447	0.133	0.314	0.248	0.247	**0.495#**	0.198	0.034	0.164
77	0.243	0.246	0.003	0.450	0.168	0.282	0.008	0.419	0.411	**0.458#**	0.173	0.285
79	**0.491#**	0.184	0.307	0.204	0.258	0.462	0.099	0.134	0.233	0.106	0.050	0.156
85	0.137	0.100	0.237	0.372	0.137	0.234	0.000	0.000	0.000	**0.371∗**	0.100	**0.472#**
88	0.270	0.277	0.008	**0.444#**	0.145	0.299	0.017	0.432	0.415	**0.462#**	0.155	0.307
93	0.109	0.255	0.146	0.158	0.111	0.047	0.460	0.240	0.220	0.301	**0.495#**	0.194
103	0.010	0.008	0.003	**0.469#**	**0.374#**	0.095	0.231	0.133	**0.363∗**	0.238	0.140	0.098
115	0.049	0.068	0.019	0.204	0.130	0.075	0.248	0.329	0.081	**0.453#**	0.397	0.056

Table 4
Classification of grains, depending on the number of slip traces evidenced by DIC. In bold, the grains for which the slip bands appear for the first time. In italics, the grains that have increased the number of active planes between two steps. Grain 103 has the particularity of activating the third active system, the first two being oriented in the same way. The grain possibly has three active sliding planes.

	Step 1	Step 2	Step 3
N° of grains with no active slip	Others	–	–
N° of grains with 1 active slip plane	**19, 31, 36, 65, 72, 85, 103, 115**	**16,** 19, 31, **46,**72,**82,** 85, **93**, **102**, 115 and others	19, 31, 46, 72, 82, 85, 93, 102, 115 and others
N° of grains with 2 active sliding planes	–	*36, 65**,***77, 79, 88,** *103**	*16,* 36, 65, 77, 79, 88, 103*

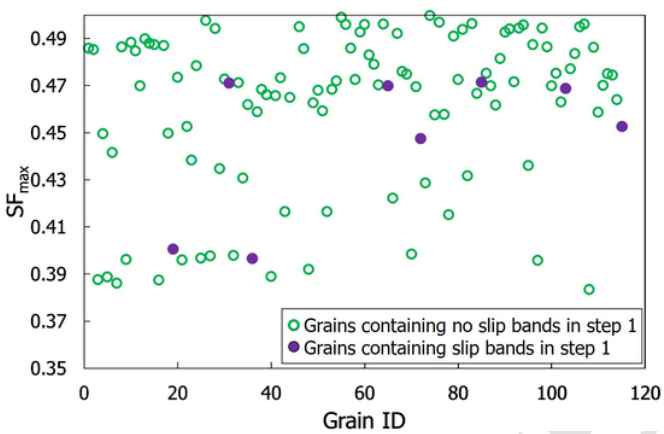

Fig. 14. Values of the maximum Schmid factor SF_{max} as a function of grain ID. Grains that do not contain a slip band appear in green, grains containing slip bands in step 1 appear in purple.

When step 2 is reached, all grains show localization bands, indicating that at least one system is active per grain. The majority of the grains have one active system and six of them have two active slip systems visible by DIC. Note that grains # 77, # 79 and # 88 had no visible slip bands for the first step but had two active slip systems for the second step. Also, among the grains with two active slip systems, the Schmid factor values of the second active slip plane are sometimes much lower than those of other grains with only one active slip system. Finally, in step 3, the majority of the activated systems are the same as in step 2; only grain # 16 has two active sliding planes.

The distribution of slip bands in the grains is then investigated. Some grains have evenly spaced bands throughout the grain (example of grains # 93 and # 115) while others have less evenly spaced bands in the grain (example of grain # 46). Also, the spacing between the sliding bands is dependent on the loading levels and the observed grain. In general, as the load increases, the spacing between the traces is decreased. At a given step, some grains show a smaller band spacing than others. For example, grains # 85 and # 103 show a small and regular band spacing compared to grain # 46. Actually, these grain have similar crystal orientation. Therefore, they have similar behaviors during the test. In the case of grain # 85, the slip planes with the maximum and 3rd maximum Schmid factor have traces actually superimposed. In the case of grain # 103, the slip planes with the maximum and 2nd maximum Schmid factor have traces actually superimposed. Thus, it is very likely that the higher density of slip bands in these grains indicates the simultaneous activity of two slip systems with the same trace.

3.3.2. Average equivalent shear strain values in grains and crystal orientation relationships

Fig. 15.a illustrates the average equivalent strain values in the grains ($\overline{\gamma_{eq}}$) for the first three loading steps. In parallel, the inverse pole figures (IPFs) are shown in Fig. 15.b. For each loading step, a distinction is made between grains with no active slip systems (green circles), those for which one slip system is active (purple circles), and those for which at least two slip systems are active (black circles). Fig. 15.c shows the IPFs with the equivalent strain values associated with each grain. From these results, there is no clear correspondence between the presence of slip bands and the average strain value in the grains. Some grains can have single or double slip bands and have low or high average equivalent strains (Fig. 15.a). During the first step, the strain is relatively homogeneous in the studied area. On the other hand, during steps 2 and 3, more marked heterogeneities are visible and some grains are much less deformed than others. From Fig. 15.b, no clear link between the grain orientation and the number of active slip systems can be seen. Similarly, in Fig. 15.c, grain orientation does not play a significant role in the average strain values in the grains.

Fig. 16 shows the calculated equivalent shear strain in each grain $\overline{\gamma_{eq}}$, at step 1, as a function of the maximum Schmid factor. No clear trend is obtained between the average value in the grains and the value of the Schmid factor. These results are similar to those obtained by Bodelot et al..[26]. Similar results are obtained for the other levels of loading.

Fig. 17 plots the average equivalent shear strain per grain in step N + 1 as a function of step N. The use of this representation allows to define if the strains measured in each grain have a link from one step to the other. If this is the case, the order established at step N will remain the same for the following steps and it is thus possible to quickly define the location where the strains will be maximal within the microstructure. In Fig. 17.a, changing from step 1 to step 2, a notable dispersion of values is observed. In other words, for small macroscopic strains, a grain that is strongly deformed at this moment is not necessarily strongly deformed later. The dispersion is reduced between step 2 and step 3 (Fig. 17.b). This result indicates that when a grain A is strongly strained at step 2 relative to a grain B, grain A will be strained even more compared to grain B at step 3. Between steps 3 and 4 (Fig. 17.c), the correlation is perfect since a purely elastic release (springback) was done at these steps.

In this paragraph, the relevance of using the parameters commonly calculated from EBSD, such as GOS and GAM, and the average equivalent shear strain, to describe the plastic activity is discussed. For this purpose, the maps of these different quantities are depicted in Fig. 18. This figure also shows the values of GOS and GAM calculated in step 4 as a function of the average equivalent shear strain in the grains. All the grains cropped by the ROI (outer grains) were not taken into account in this representation. Very scattered results are obtained and no major relationship can be established between the parameters measured in EBSD and the equivalent shear strains measured in the grains. These results are similar to those reported by Bourquerel et al. [48]. Indeed the latter, they showed that the relationship between GOS and applied strain values is very scattered. Nevertheless, it is noticeable that the average value of the GOS parameter in the studied area increased during the tensile test, from 1.6° to 3.3° which is consistent with what has been previously observed in the literature for other types of materials [49, 50]. The EBSD parameters chosen in this work therefore imply that the GAM and GOS parameters can be used globally, to quantify the macroscopic strain. On the other hand, it is not possible to rely on the values obtained for each grain to define the average strains.

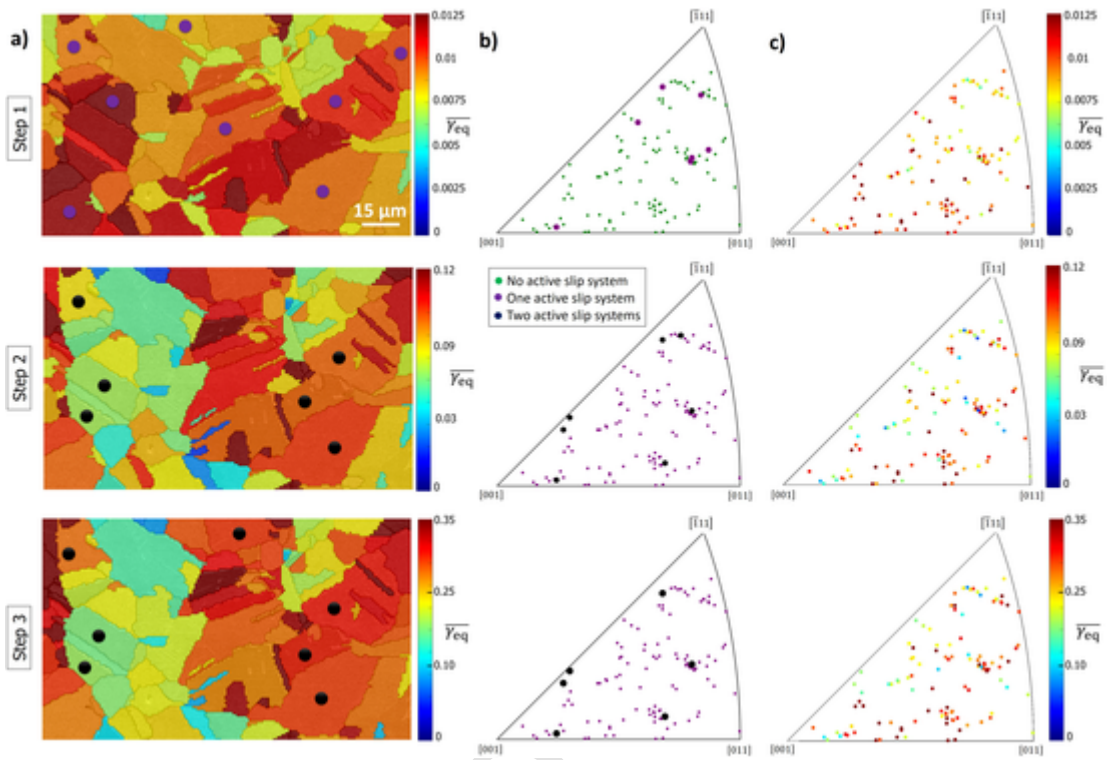

Fig. 15. a) Maps of $\overline{\gamma_{eq}}$ values, b) and c) inverse pole figures of *x* direction, for the three first steps. Green circles represent the grains with no active slip system. Purple circles represent grains with one active slip system. The black circles represent grains with at least two active slip systems.

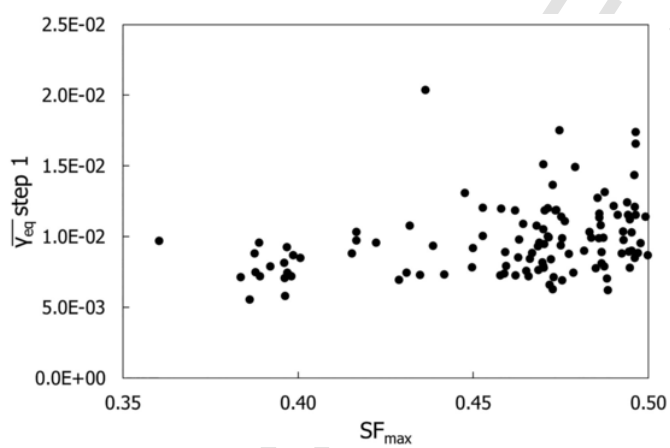

Fig. 16. Effective shear strain in each grain $\overline{\gamma_{eq}}$ calculated in step 1, as a function of maximum Schmid factor SF_{max}.

4. Discussion

As stated in the introduction, the tests conducted prior to modeling must offer representative data on macroscopic behavior in order to quickly determine the parameters of a polycrystalline model. As a result, the size of the ROI, the required image resolution, and the variables to be included in the analysis are all key considerations in solving the problem.

4.1. Minimal grains number in ROI

If the selected ROI size appeared to be sufficient with respect to the results presented in Section 3.1, it would be interesting to know if the ROI could be even smaller. The characterization of a too small ROI could lead to a wrong interpretation of the results and, subsequently, to an identification of the polycrystalline model parameters that are not representative of the macroscopic behavior. On the other hand, choosing a ROI that is too large would lead to an increase in measurement and computational time.

In order to evaluate the impact of the number of grains on the results, the average values calculated for each grain ($\overline{\gamma_{eq}}$) was used. An average value $\langle\overline{\gamma_{eq}}\rangle$ was calculated by randomly considering 2 to 115 grains. The standard deviation associated with these average values is

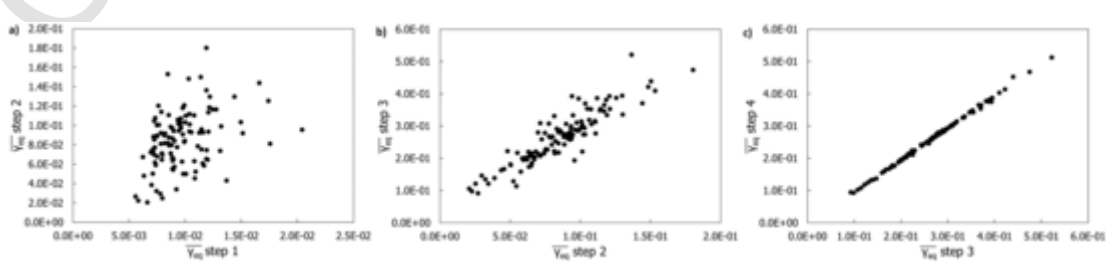

Fig. 17. Evolution of the average equivalent shear strain calculated for each grain $\overline{\gamma_{eq}}$ for step N + 1 as a function of step N.

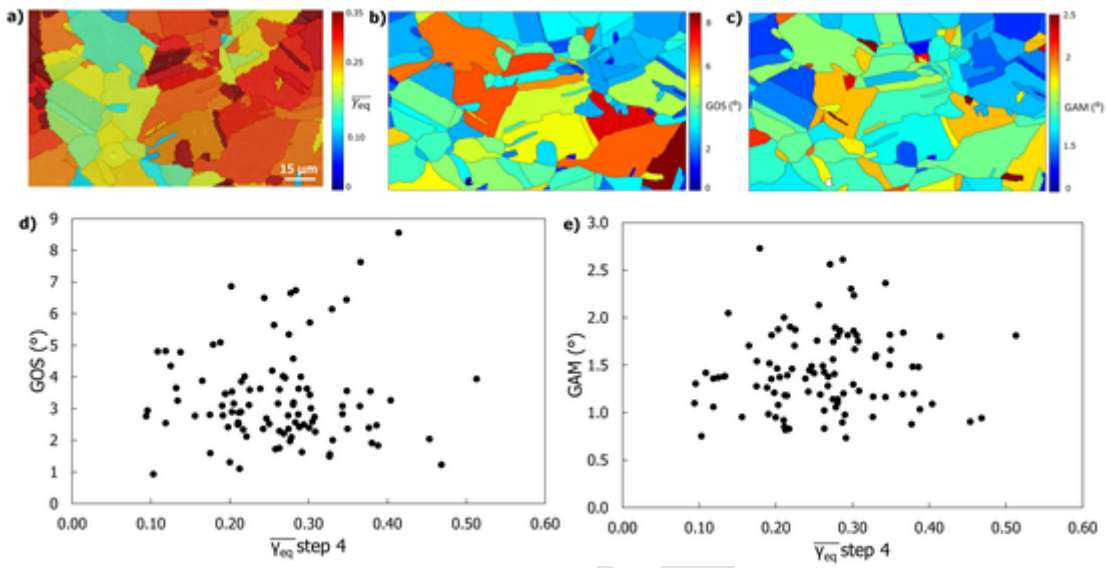

Fig. 18. Maps of a) $\overline{\gamma_{eq}}$, b) GOS and c) GAM for step 4. Relationship between d) GOS and $\overline{\gamma_{eq}}$ and between e) GAM and $\overline{\gamma_{eq}}$.

also calculated. The overall results are shown in Fig. 19 for the first three loading steps. The impact of the number of grains considered in the calculation is limited with regard to the evolution of the average values and standard deviations. As soon as more than 20 grains are considered, the mean value evolves in small amount and this is independent of the loading. The standard deviation also fluctuates a little as the number of grains increases. These results are not very surprising in view of the $\overline{\gamma_{eq}}$ maps shown in Fig. 16, where the grains have relatively close mean values.

Another criterion to select the ROI was investigated. Depending on the size of the ROI, the number of grains n and the change in ODF ($\Delta\mathrm{ODF}_n$) were recorded, as summed in Fig. 20. This procedure was repeated until $n = 450$. For a given n, the difference between the corresponding change in ODF and the reference one (that with $n = 450$) was characterized in terms of texture index (TI):

$$\mathrm{TI} = \oint \left[\Delta\mathrm{ODF}_n - \Delta\mathrm{ODF}_{450}\right]^2 \mathrm{d}E \tag{11}$$

where E denotes the Euler space. A TI near zero means that the texture between the two microstructures are very close. Fig. 20 represents the evolution of the TI as a function of the number of grains. The TI decreases significantly when the number of grains is increased up to 50. After this value, it is less than 0.25 and evolves slowly, the TI varied by less than 20%. These results suggest that a minimum grain number to consider for analysis could be 50.

4.2. Window size of analysis

The choice of experimental parameters to define the strain fields was discussed in Section 3.1. The conclusion was to retain a window size of $\varphi_{\mathrm{window}}$ equal to 1.3 µm in order to be able to visualize the slip bands and not be disturbed by aberrant values that can be generated by these slip bands. This window size corresponds to a factor of 10 compared to the width of the slip bands observed by SEM. The visualization of the slip bands brings much information in addition to the EBSD data as expressed in Section 3.3 (related to the Schmid factor, the number of active slip systems, …). It appears, therefore, relevant to make this choice when a purely experimental analysis is performed. This choice is more questionable when the objective is to compare strain fields obtained with experiments and modeling. The CPFE models do not allow the visualization of slip localization. Using such a small size of $\varphi_{\mathrm{window}}$ appears pointless. In this case, the use of an intermediate scale appears more appropriate. A window size $\varphi_{\mathrm{window}}$ equal to 9.6 µm allows to visualize the major strains generated inside the grains and between them (see Fig. 6). When setting up a coupling with the model, we prefer to select a $\varphi_{\mathrm{window}}$ of the order of the grain size.

4.3. Variables of interest

In Section 3.3, many variables were calculated in relation to the data obtained in DIC and EBSD. From the DIC data, the equivalent shear strain γ_{eq} was used to represent and interpret the results. This choice is somewhat different from the one made by Di Gioacchino et al. [6] to in-

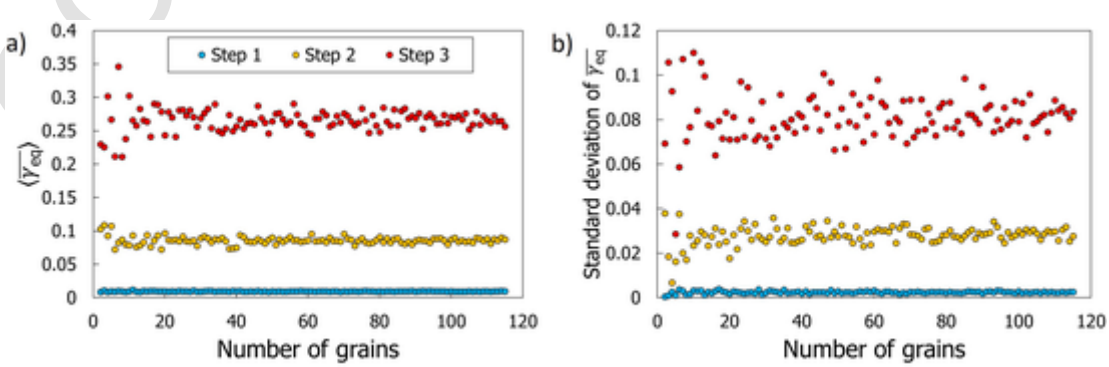

Fig. 19. a) Evolution of $\langle\overline{\gamma_{eq}}\rangle$ as a function of the number of grains. b) Standard deviation of the mean value of $\overline{\gamma_{eq}}$ as a function of the number of grains.

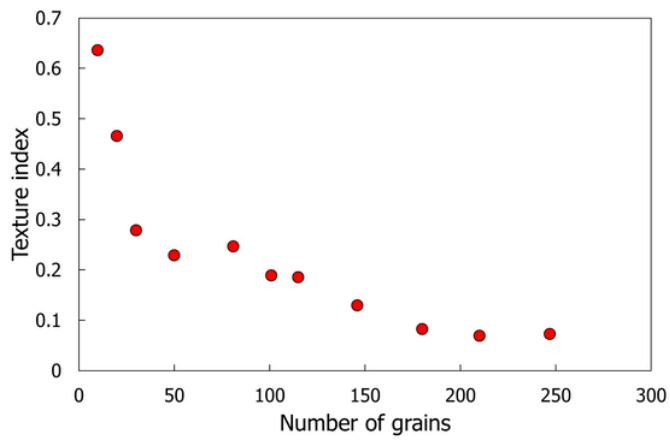

Fig. 20. Evolution of the texture index, as defined in (11), as a function of the number of grains.

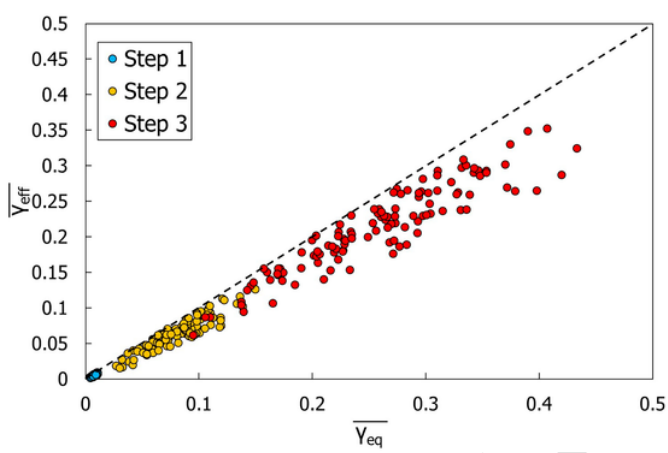

Fig. 21. Comparison of $\overline{\gamma_{eff}}$ and $\overline{\gamma_{eq}}$ values for the first 3 steps.

troduce the effective shear strain γ_{eff} (Eq. (7)). The whole data set was used to compare the two variables.

Fig. 21 compares the average values of effective shear strain $\overline{\gamma_{eff}}$ and equivalent shear strain $\overline{\gamma_{eq}}$ calculated in each grain for the first three steps. Some fluctuations are observed between the two variables but a clear trend is obtained. For all values, the effective shear strain is lower than the equivalent shear strain. The two variables were also compared with respect to the fields obtained. They are represented for step 3 in Fig. 22. Except for the amplitude, the maps are very similar. These results show that both quantities are able to evidence the localization bands. Considering γ_{eq} or γ_{eff} seems of limited importance. It seems, nevertheless, more judicious to take as a comparison variable the γ_{eq} variable because the formulation is also valid in large strains (see Section 2.4).

The GOS and GAM values computed from EBSD after performing the test do not show a clear correspondence with the calculated average shear strains in the grains $\overline{\gamma_{eq}}$. Therefore, they cannot be used as accurate comparison points. Moreover, it was shown from DIC analyses that the Schmid factor alone does not completely define its average values in the grains as well as the active slip systems. The characterization of the slip bands by DIC can thus appear as an interesting point of comparison with the modeling. Indeed, although the visualization of the slip bands is not possible with the CPFE modeling, it is quite possible to extract from the modeling the active slip systems and thus compare them with the experiment. Moreover, it was shown that the spacing between slip bands could be a characteristic of the activation of several slip systems defining a similar trace. Systematic characterization of this parameter could provide another point of comparison when implementing the modeling to define the active slip systems.

5. Summary and conclusion

An in situ SEM tensile test was carried out on pure copper. Macroscopic curve, HRDIC measurements and EBSD measurements were then used to define the main characteristics of the tensile behavior of this material. The analysis of the equivalent shear strain, coupled with the EBSD data, led to the following conclusions:

- The traces of slip planes evidenced by DIC are in agreement with the maximum Schmid factors calculated by considering a macroscopic stress as boundary conditions.
- More than 90% of the grains show a single slip trace, indicating that for most of the grains, the Schmid factor drives the most active slip plane.
- Strain calculations for each grain indicate that the strains are relatively homogeneous for the first step of loading but strain inhomogeneity develops in subsequent steps.

Moreover, the experimental approach implemented in this work has allowed successively: to define the parameters of correlation of digital images to be used to observe the heterogeneities of strain in the grains, to define the region of interest and to analyze the results obtained in this area. The main information to remember is listed below:

- Two DIC windows should be used depending on the observations one wishes to make. The DIC window must be of the order of 10 times the width of the slip bands if the wish is to visualize them and define their spacing. The DIC window must be of the order of the grain size when the objective is to compare the results to modeling.
- The minimum number of grains to consider for the analysis of the results is 50. The same is true for the implementation of the modeling.
- The variables of interest for the analysis of the results and the comparison with the modeling is γ_{eq}. This variable is used to highlight the slip bands (depending on the choice of the window selected). The spacing between the slip bands can also be

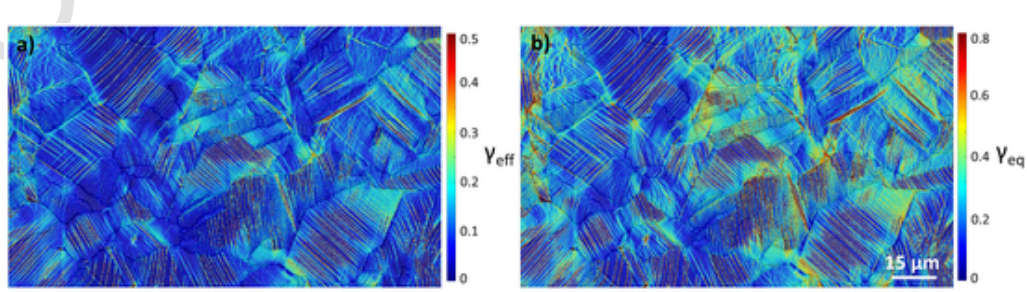

Fig. 22. Comparison of maps of a) $\overline{\gamma_{eff}}$ and b) $\overline{\gamma_{eq}}$ for the step 3. Window size $\varphi_{window} = 0.54$ µm.

representative of the number of active slip systems and thus serve as a point of comparison with the model.

Data availability

The raw/processed data required to reproduce these findings cannot be shared at this time as the data also forms part of an ongoing study.

CRediT authorship contribution statement

J.P. Goulmy : Conceptualization, Investigation, Writing – original draft. **D. Depriester :** Software, Validation, Formal analysis, Writing – original draft. **F. Guittonneau :** Investigation, Writing – review & editing. **L. Barrallier :** Writing – review & editing, Supervision. **S. Jégou :** Writing – review & editing.

Declaration of Competing Interest

The authors declare that they have no known competing financial interests or personal relationships that could have appeared to influence the work reported in this paper.

Data availability

Data will be made available on request.

Appendix A. Equivalent strain under the generalized plane strain assumption

We assume that the material undergoes a combination of plane-strain deformation associated with out-of-plane stretch, as illustrated in Fig. 23. This state is usually referred to as the generalized plane strain. In this case, the gradient tensor is:

$$F = \begin{bmatrix} F_{11} & F_{12} & 0 \\ F_{21} & F_{22} & 0 \\ 0 & 0 & F_{33} \end{bmatrix} \tag{12}$$

If the strain is purely plastic, it can be considered as perfectly isochoric. Thus, the volumetric change is [51, Chap. 2]:

$$\frac{\Delta v}{V} = \det F - 1 = 0 \tag{13}$$

Therefore:

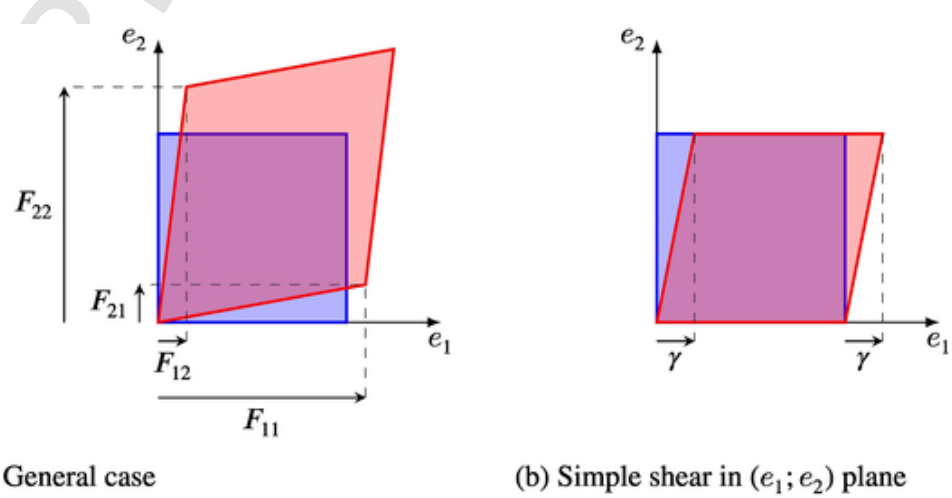

Fig. 23. 2D representation of strain: the blue square, of unit size, illustrates the reference geometry whereas the red area illustrates the deformed geometry.

$$F_{33} = \frac{1}{F_{11}F_{22} - F_{12}F_{21}} \tag{14}$$

The Green–Lagrange (GL) tensor is:

$$E = \frac{1}{2}\left(F^{\top}\cdot F - \delta\right) \tag{15}$$

$$= \frac{1}{2}\begin{bmatrix} F_{11}^2 + F_{21}^2 - 1 & F_{11}F_{12} + F_{21}F_{22} & 0 \\ F_{11}F_{12} + F_{21}F_{22} & F_{12}^2 + F_{22}^2 - 1 & 0 \\ 0 & 0 & F_{33}^2 - 1 \end{bmatrix} \tag{16}$$

The deviatoric part of the GL tensor is:

$$\breve{E} = E - \frac{1}{3}\mathrm{tr}\,(E)\,\delta \tag{17}$$

$$= \frac{1}{3}\begin{bmatrix} 2E_{11} - E_{22} - E_{33} & 3E_{12} & 0 \\ 3E_{12} & -E_{11} + 2E_{22} - E_{33} & 0 \\ 0 & 0 & -E_{11} - E_{22} + 2E_{33} \end{bmatrix} \tag{18}$$

It comes:

$$\mathrm{tr}\left(\breve{E}^2\right) = \frac{(2E_{11} - E_{22} - E_{33})^2 + (-E_{11} + 2E_{22} - E_{33})^2 + (-E_{11} - E_{22} + 2E_{33})^2}{9} + 2E_{12}^2 \tag{19}$$

$$= \frac{2}{3}\left(E_{11}^2 + E_{22}^2 + E_{33}^2 - E_{11}E_{22} - E_{11}E_{33} - E_{22}E_{33}\right) + 2E_{12}^2 \tag{20}$$

$$= \frac{\left(E_{11} - E_{22}\right)^2 + \left(E_{11} - E_{33}\right)^2 + \left(E_{22} - E_{33}\right)^2}{3} + 2E_{12}^2 \tag{21}$$

Hence, the von Mises equivalent strain is:

$$\varepsilon_{\mathrm{eq}} = \sqrt{\frac{2}{3}\breve{E} : \breve{E}} \tag{22}$$

$$= \sqrt{\frac{2}{3}}\sqrt{\frac{(E_{11} - E_{22})^2 + (E_{11} - E_{33})^2 + (E_{22} - E_{33})^2}{3} + 2E_{12}^2} \tag{23}$$

Now, let us consider a medium undergoing simple shear, as illustrated in Fig. 23. In this case, we have:

$$F = \begin{bmatrix} 1 & \gamma & 0 \\ 0 & 1 & 0 \\ 0 & 0 & 1 \end{bmatrix} \tag{24}$$

$$E = \begin{bmatrix} 0 & \frac{\gamma}{2} & 0 \\ \frac{\gamma}{2} & \frac{\gamma^2}{2} & 0 \\ 0 & 0 & 1 \end{bmatrix} \tag{25}$$

Therefore, Eq. (23) becomes:

$$\varepsilon_{\mathrm{eq}} = \frac{\gamma}{\sqrt{3}}\sqrt{1 + \frac{\gamma^2}{3}} \tag{26}$$

This relationship is similar to that proposed by Shrivastava et al. [52], and both are equivalent if γ is small (if $-0.5<\gamma<0.5$, the relative error is below 4%). If $\gamma \geqslant 0$, Eq. (26) can be inverted, leading to:

$$\gamma = \sqrt{\frac{3}{2}}\sqrt{\sqrt{1 + 4\varepsilon_{\mathrm{eq}}^2} - 1} \tag{27}$$

References

[1] J.C. Stinville, W.C. Lenthe, J. Miao, T.M. Pollock, Acta Materialia 103 (2016) 461–473 https://doi.org/10.1016/j.actamat.2015.09.050, URL:https://www.sciencedirect.com/science/article/pii/S1359645415007399.

[2] J.M. Hestroffer, M.I. Latypov, J.-C. Stinville, M.-A. Charpagne, V. Valle, M.P. Miller, T.M. Pollock, I.J. Beyerlein, Acta Materialia 226 (2022) 117627 https://doi.org/10.1016/j.actamat.2022.117627, URL:https://linkinghub.elsevier.com/retrieve/pii/S1359645422000118.

[3] J.-C. Stinville, W.C. Lenthe, M.P. Echlin, P.G. Callahan, D. Texier, T.M. Pollock, International Journal of Fracture 208 (2017) 221–240 https://doi.org/10.1007/s10704-017-0241-z, URL:https://hal.archives-ouvertes.fr/hal-01662675, publisher: Springer Verlag.

[4] M. Charpagne, J. Stinville, P. Callahan, D. Texier, Z. Chen, P. Villechaise, V. Valle, T. Pollock, Materials Characterization 163 (2020) 110245 https://doi.org/

10.1016/j.matchar.2020.110245, URL:https://linkinghub.elsevier.com/retrieve/pii/S1044580319335569.
[5] M.I. Latypov, J.-C. Stinville, J.R. Mayeur, J.M. Hestroffer, T.M. Pollock, I.J. Beyerlein, Scripta Materialia 192 (2021) 78–82 https://doi.org/10.1016/j.scriptamat.2020.10.001, URL:https://www.sciencedirect.com/science/article/pii/S1359646220306448.
[6] F. Di Gioacchino, J. Quinta da Fonseca, International Journal of Plasticity 74 (2015) 92–109 https://doi.org/10.1016/j.ijplas.2015.05.012, URL:http://www.sciencedirect.com/science/article/pii/S0749641915000820.
[7] J. Stinville, P. Echlin, D. Texier, F. Bridier, P. Bocher, T. Pollock, Experimental Mechanics 56 (2016) 197–216 https://doi.org/10.1007/s11340-015-0083-4, URL: https://hal.archives-ouvertes.fr/hal-01644841, publisher: Society for Experimental Mechanics.
[8] A.W. Mello, T.A. Book, A. Nicolas, S.E. Otto, C.J. Gilpin, M.D. Sangid, Experimental Mechanics 57 (2017) 1395–1409, https://doi.org/10.1007/s11340-017-0303-1.
[9] Y. Guan, B. Chen, J. Zou, T.B. Britton, J. Jiang, F.P.E. Dunne, International Journal of Plasticity 88 (2017) 70–88 https://doi.org/10.1016/j.ijplas.2016.10.001, URL:https://www.sciencedirect.com/science/article/pii/S0749641916301978.
[10] R. Thomas, D. Lunt, M.D. Atkinson, J. Quinta da Fonseca, M. Preuss, F. Barton, J. O'Hanlon, P. Frankel, Materialia 5 (2019) 100248 https://doi.org/10.1016/j.mtla.2019.100248, URL:https://www.sciencedirect.com/science/article/pii/S2589152919300444.
[11] J.C. Stinville, P.G. Callahan, M.A. Charpagne, M.P. Echlin, V. Valle, T.M. Pollock, Acta Materialia 186 (2020) 172–189 https://doi.org/10.1016/j.actamat.2019.12.009, URL:http://www.sciencedirect.com/science/article/pii/S1359645419308389.
[12] F. Di Gioacchino, T.E.J. Edwards, G.N. Wells, W.J. Clegg, Scientific Reports 10 (2020) 10082 https://doi.org/10.1038/s41598-020-66569-7, URL:http://www.nature.com/articles/s41598-020-66569-7.
[13] N.I. Thiruselvam, R. Jeyaraam, S.J. Subramanian, S. Sankaran, Materialia 18 (2021) 101164 https://doi.org/10.1016/j.mtla.2021.101164, URL:https://www.sciencedirect.com/science/article/pii/S2589152921001678.
[14] X.X. Guan, L. Lu, S.N. Luo, D. Fan, Materials Science and Engineering: A 813 (2021) 141073 https://doi.org/10.1016/j.msea.2021.141073, URL:https://www.sciencedirect.com/science/article/pii/S0921509321003427.
[15] R. Sperry, S. Han, Z. Chen, S.H. Daly, M.A. Crimp, D.T. Fullwood, Materials Characterization 173 (2021) 110941 https://doi.org/10.1016/j.matchar.2021.110941, URL: https://www.sciencedirect.com/science/article/pii/S1044580321000711.
[16] F. Delaire, J.L. Raphanel, C. Rey, Acta Materialia 48 (2000) 1075–1087 https://doi.org/10.1016/S1359-6454(99)00408-5, URL:https://www.sciencedirect.com/science/article/pii/S1359645499004085.
[17] M.A. Sutton, N. Li, D.C. Joy, A.P. Reynolds, X. Li, Experimental Mechanics 47 (2007) 775–787, https://doi.org/10.1007/s11340-007-9042-z.
[18] M.A. Sutton, N. Li, D. Garcia, N. Cornille, J.-J. Orteu, S.R. McNeill, H.W. Schreier, X. Li, A.P. Reynolds, Experimental Mechanics 47 (2007) 789–804 https://doi.org/10.1007/s11340-007-9041-0, URL:https://hal.archives-ouvertes.fr/hal-01644895, publisher: Society for Experimental Mechanics.
[19] C. Mansilla, V. Ocelík, J.T.M.D. Hosson, Microscopy and Microanalysis 20 (2014) 1625–1637 https://doi.org/10.1017/S1431927614013282, URL:https://www.cambridge.org/core/journals/microscopy-and-microanalysis/article/new-methodology-to-analyze-instabilities-in-sem-imaging/DD22BA1A8525A968AF0FED7AB5166471.
[20] A. Guery, F. Hild, F. Latourte, S. Roux, Mechanics of Materials 100 (2016) 55–71 https://doi.org/10.1016/j.mechmat.2016.06.007, URL: https://linkinghub.elsevier.com/retrieve/pii/S0167663616300813.
[21] J.-C. Stinville, T. Francis, A. Polonsky, C. Torbet, Z. Chen, G. Balbus, F. Bourdin, V. Valle, P. Callahan, M. Echlin, M.-A. Charpagne, T.M. Pollock, Experimental Mechanics (2020), https://doi.org/10.1007/s11340-020-00632-2.
[22] C. Blochwitz, J. Brechbühl, W. Tirschler, Materials Science and Engineering: A 210 (1996) 42–47 https://doi.org/10.1016/0921-5093(95)10076-8, URL:https://www.sciencedirect.com/science/article/pii/0921509395100768.
[23] A. El Bartali, V. Aubin, L. Sabatier, P. Villechaise, S. Degallaix-Moreuil, Scripta Materialia 59 (2008) 1231–1234 https://doi.org/10.1016/j.scriptamat.2008.07.044, URL: https://www.sciencedirect.com/science/article/pii/S1359646208005630.
[24] N.L. Phung, V. Favier, N. Ranc, International Journal of Fatigue 77 (2015) 115–127 https://doi.org/10.1016/j.ijfatigue.2015.03.009, URL: https://www.sciencedirect.com/science/article/pii/S0142112315000687.
[25] Z. Zhang, D. Lunt, H. Abdolvand, A.J. Wilkinson, M. Preuss, F.P.E. Dunne, International Journal of Plasticity 108 (2018) 88–106 https://doi.org/10.1016/j.ijplas.2018.04.014, URL: https://www.sciencedirect.com/science/article/pii/S0749641917307064.
[26] L. Bodelot, Experimental Mechanics 59 (2019) 691–702, https://doi.org/10.1007/s11340-019-00508-0.
[27] F. Di Gioacchino, J. Quinta da Fonseca, Experimental Mechanics 53 (2013) 743–754, https://doi.org/10.1007/s11340-012-9685-2.
[28] A. Guery, F. Hild, F. Latourte, S. Roux, International Journal of Plasticity 81 (2016) 249–266 https://doi.org/10.1016/j.ijplas.2016.01.008, URL:https://www.sciencedirect.com/science/article/pii/S0749641916000188.
[29] A. Lakshmanan, J. Luo, I. Javaheri, V. Sundararaghavan, International Journal of Plasticity 142 (2021) 102991 https://doi.org/10.1016/j.ijplas.2021.102991, URL: https://www.sciencedirect.com/science/article/pii/S0749641921000668.
[30] C.S. Patil, S. Chakraborty, S.R. Niezgoda, International Journal of Plasticity 147 (2021) 103099 https://doi.org/10.1016/j.ijplas.2021.103099, URL:https://www.sciencedirect.com/science/article/pii/S0749641921001698.
[31] T. Yalcinkaya, I. özdemir, I. Tarik Tandogan, Computational Mechanics 67 (2021) 937–954 https://doi.org/10.1007/s00466-021-01972-z, URL: http://link.springer.com/10.1007/s00466-021-01972-z.
[32] H.-R. Wenk, P.V. Houtte, Reports on Progress in Physics 67 (2004) 1367–1428 https://doi.org/10.1088/0034-4885/67/8/R02, URL:https://doi.org/10.1088/0034-4885/67/8/r02, publisher: IOP Publishing.
[33] P. Van Houtte, S. Li, M. Seefeldt, L. Delannay, International Journal of Plasticity 21 (2005) 589–624 https://doi.org/10.1016/j.ijplas.2004.04.011, URL:https://www.sciencedirect.com/science/article/pii/S0749641904000610.
[34] H. Wang, C. Lu, K. Tieu, Y. Liu, Journal of Materials Science & Technology 76 (2021) 231–246 https://doi.org/10.1016/j.jmst.2020.10.020, URL:https://www.sciencedirect.com/science/article/pii/S1005030220308847.
[35] S. Sun, V. Sundararaghavan, International Journal of Solids and Structures 51 (2014) 3350–3360 https://doi.org/10.1016/j.ijsolstr.2014.05.027, URL:https://www.sciencedirect.com/science/article/pii/S0020768314002212.
[36] J. Luo, V. Sundararaghavan, International Journal of Solids and Structures 150 (2018) 197–207 https://doi.org/10.1016/j.ijsolstr.2018.06.015, URL:https://www.sciencedirect.com/science/article/pii/S0020768318302476.
[37] G. Sachs, in: O. Bauer, M. Hansen, F.v. Göler, G. Sachs, E. Schmid, G. Wassermann, K. Sipp, H. Sieglerschmidt, R. Karnop, W. Kuntze, K. Laute, R. Eisenschitz, B. Rabinowitsch, K. Weissenberg, W. Boas, M. Masima (Eds.), Mitteilungen der deutschen Materialprüfungsanstalten: Sonderheft IX: Arbeiten aus dem Kaiser Wilhelm-Institut für Metallforschung und demStaatlichen Materialprüfungsamt zu Berlin-Dahlem, Springer, Berlin, Heidelberg, 1929, pp. 94–97, https://doi.org/10.1007/978-3-642-92045-5_12.
[38] G.I. Taylor, J. Inst. Metals 62 (1938) 307–324 URL: https://ci.nii.ac.jp/naid/10026664057/.
[39] Q. Shi, S. Roux, F. Latourte, F. Hild, D. Loisnard, N. Brynaert, Ultramicroscopy, Part A 184 (2018) 71–87 https://doi.org/10.1016/j.ultramic.2017.08.005, URL: https://hal.archives-ouvertes.fr/hal-01674581, publisher: Elsevier.
[40] J. Goulmy, S. Jégou, L. Barrallier, Optics & Laser Technology 148 (2022) 107792 https://doi.org/10.1016/j.optlastec.2021.107792, URL:https://linkinghub.elsevier.com/retrieve/pii/S003039922100880X.
[41] S. Preibisch, S. Saalfeld, P. Tomancak, Bioinformatics 25 (2009) 1463–1465 https://doi.org/10.1093/bioinformatics/btp184, URL:https://www.ncbi.nlm.nih.gov/pmc/articles/PMC2682522/.
[42] F. Bachmann, R. Hielscher, H. Schaeben, Ultramicroscopy 111 (2011) 1720–1733 https://doi.org/10.1016/j.ultramic.2011.08.002, URL:https://www.sciencedirect.com/science/article/pii/S0304399111001951.
[43] A.J. Schwartz, M. Kumar, B.L. Adams, D.P. Field, Electron backscatter diffraction in materials science, volume 2, Springer, 2009.
[44] S.I. Wright, M.M. Nowell, D.P. Field, Microscopy and Microanalysis 17 (2011) 316–329 https://doi.org/10.1017/S1431927611000055, URL:https://www.cambridge.org/core/journals/microscopy-and-microanalysis/article/review-of-strain-analysis-using-electron-backscatter-diffraction/5318630F3BF9A8AB3C9ABD63C46F6698.
[45] J. Blaber, B. Adair, A. Antoniou, Experimental Mechanics 55 (2015) 1105–1122 https://doi.org/10.1007/s11340-015-0009-1, URL:http://link.springer.com/10.1007/s11340-015-0009-1.
[46] Y. Li, L. Zhu, Y. Liu, Y. Wei, Y. Wu, D. Tang, Z. Mi, Journal of the Mechanics and Physics of Solids 61 (2013) 2588–2604 https://doi.org/10.1016/j.jmps.2013.08.007, URL:https://www.sciencedirect.com/science/article/pii/S002250961300152X.
[47] L.R. Chen, X.Z. Xiao, L. Yu, H.J. Chu, H.L. Duan, Proceedings of the Royal Society A: Mathematical, Physical and Engineering Sciences 474 (2018) 20170604 https://doi.org/10.1098/rspa.2017.0604, URL:https://royalsocietypublishing.org/doi/10.1098/rspa.2017.0604, publisher: Royal Society.
[48] J. Bouquerel, C. Schayes, J.B. Vogt, Materials Science and Engineering: A 820 (2021) 141454 https://doi.org/10.1016/j.msea.2021.141454, URL:https://www.sciencedirect.com/science/article/pii/S0921509321007231.
[49] F. Wagner, N. Allain-Bonasso, S. Berbenni, D.P. Field, Materials Science Forum 702–703 (2011) 245–252 URL:https://www.academia.edu/32688567/On_the_Use_of_EBSD_to_Study_the_Heterogeneity_of_Plastic_Deformation.
[50] J.P. Goulmy, E. Rouhaud, P. Kanoute, L. Toualbi, S. Kruch, V. Boyer, J. Badreddine, D. Retraint, Materials Characterization 175 (2021) 111067 https://doi.org/10.1016/j.matchar.2021.111067, URL:https://www.sciencedirect.com/science/article/pii/S1044580321001972.
[51] S. Nemat-Nasser, Plasticity: a treatise on finite deformation of heterogeneous inelastic materials, Cambridge University Press, 2004.
[52] S. Shrivastava, J. Jonas, G. Canova, Journal of the Mechanics and Physics of Solids 30 (1982) 75–90 https://doi.org/10.1016/0022-5096(82)90014-X, URL: https://www.sciencedirect.com/science/article/pii/002250968290014X.